IEEE Access
Multidisciplinary | Rapid Review | Open Access Journal

Received 27 February 2023, accepted 13 March 2023, date of publication 24 March 2023, date of current version 30 April 2024.

Digital Object Identifier 10.1109/ACCESS.2023.3261661

Volume Conservation Constrained Multi-Material Reconstruction for Inconsistent Spectral CT Imaging

XIAOHUAN YU, AILONG CAI, NINGNING LIANG, SHAOYU WANG, LEI LI, AND BIN YAN

Henan Key Laboratory of Imaging and Intelligent Processing, PLA Strategic Support Force Information Engineering University, Zhengzhou 450001, China

Corresponding author: Bin Yan (ybspace@hotmail.com)

This work was supported in part by the National Natural Science Foundation of China under Grant 62101596 and Grant 62201616, in part by the National Key Research and Development Project of China under Grant 2020YFC1522002, and in part by the China Postdoctoral Science Foundation under Grant 2019M663996.

ABSTRACT Spectral computed tomography (spectral CT) is a promising medical imaging technology because of its ability to provide information on material characterization and quantification. However, the difficulty of decomposition increases due to the nonlinearity of the measurements and the ill-condition of the problem, especially in the case of geometric inconsistency, which typically leads to low image qualities. Therefore, it is a crucial issue for inconsistent spectral CT imaging to improve the accuracy of material decomposition while suppressing noise. This paper proposes one-step multi-material algorithms based on a statistical reconstruction model with different priors. In these approaches, the gradient sparsity based and convolutional neural network based methods are designed for the case of the consistent numbers of material and energies. Furthermore, volume conservation constraint is developed while the two numbers are not equal. An efficient Newton descent method is adopted based on a simple surrogate function. For simulation experiments with different noise levels, the largest peak signal-to-noise ratio (PSNR) obtained by the proposed method approximately increases by 20.924 dB and 18.283 dB compared with those of other algorithms. Magnified areas of real data also demonstrated that the proposed methods have a better ability to suppress noise. Numerical experiments verify that the proposed methods efficiently reconstruct the material maps and reduced noise compared with the state-of-the-art methods.

INDEX TERMS Spectral computed tomography, image reconstruction, one-step material decomposition, inconsistent geometry.

I. INTRODUCTION

Spectral computed tomography (spectral CT) has promising potential in wide applications due to its ability to quantitative material discrimination for diagnostics and therapy evaluation in medical imaging [1], [2], [3]. Evidence is emerging to suggest that spectral CT can help to improve the diagnosis of coronavirus disease (COVID-19) [4], [5]. As one of the typical implementations of spectral CT, the principle of dual-energy CT (DECT) has been studied for a long time. Recent developments in energy-selective detectors have spurred research in this area, especially improvements in photon-counting detectors (PCDs) [6]. However, low signal-to-noise ratio (SNR) measurements, caused by pile-up, fluorescence effect, charge sharing, and photon scattering, affect the image quality as well as the accuracy of material decomposition [7]. In the imaging process, quantum noise, electronic noise and reconstruction noise introduced by hardware devices and algorithms will degrade our imaging results. As well as the development of equipment, optimizing algorithms and parameters are critical in the field of medical imaging to improve the accuracy of material decomposition and maintain image quality.

In recent years, there are two categories of methods for reconstructing material-specific images: two-step methods and one-step methods. Furthermore, the

The associate editor coordinating the review of this manuscript and approving it for publication was Essam A. Rashed.

two-step methods can be divided into image-domain and projection-domain based methods. In image-domain based approaches [8], [9], [10], [11], CT images are first reconstructed from polychromatic projection data, followed by a decomposition step to obtain the corresponding material images. Unfortunately, the quality of material results is often severely impacted by beam-hardening artifacts and noise explosions caused by direct matrix inversion-based decomposition, especially when there are more than two materials to be separated [12]. In contrast, projection-domain based methods involve separating or decomposing the multi-energy projections into material-specific projections, before reconstructing them through traditional algorithms [13], [14], [15]. However, it requires the projection in multi-energy measured under strictly consistent and identical imaging geometry (i.e., the same source, object, and detector positions), which limits its application in fast kVp switching [16] or multi-source-multi-detector [17] systems. Additionally, the material-specific results of two-step methods depend on the quality of the first step, and it is difficult for the second step to compensate for the errors caused by the first step.

To avoid these problems in dual material imaging with dual spectral CT, several methods have been proposed that aim to directly obtain material-specific images from the nonlinear observation measurements. These methods, referred to as one-step iterative methods, typically combine forward models of the reconstruction with the material separation process. For instance, Zhao et al. utilized the first-order Taylor expansion of nonlinear observations and proposed an extended algebraic reconstruction technique (EART) [18] for DECT. In recent years, several variants of EART have been developed for improving convergence efficiency, such as the simultaneous EART (ESART) [19], the monochromatic images guided iteration method [20] for dual-energy, which accelerates the convergence but needs to manually determine the optimal values of reference energy. And the oblique projection modification technique (OPMT) [21] for inconsistent scanning to acquire the material-specific maps. In addition, as the photons emitted by X-ray source often contain statistical significance, different statistical iterative methods have also emerged. Qiong et al. [22] have developed a penalized-likelihood algorithm to carry out basis materials decomposition for DECT. Several other researchers, such as Long et al. [23], Weidinger et al. [24] and Mechlem et al. [25], have designed separable quadratic surrogates of spectral CT statistical models to achieve a one-step material decomposition. Barber et al. [26] applied primal-dual prototype framework to material imaging of spectral CT. Very recently, they further proposed to investigate the convergence theory of the nonconvex alternating direction of multipliers method (NcADMM) [27] and conducted the reconstruction of the PCD system to reduce beam-hardening and metal artifacts [28]. It is more challenging to solve the inverse problem when the occasion comes into an inconsistent scanning system.

Moreover, due to the inherent ill-conditioning of the CT inverse problem, it is often necessary to incorporate prior knowledge as a regularization term to suppress the noise of basis material images. To further enhance the quality of reconstruction, sparsity-based methods have been employed. For example, Cai et al. [29] adopted the Huber function [30] as the regularization term in a Bayesian approach. Chen et al. [31], [32] applied the convex indicator function of the gradient image to enforce an upper bound on the material images and monochromatic images. Zhang et al. [33] proposed a direct material reconstruction method that combined total variation (TV) and block-matching and 3D filtering for DECT. However, some of the above-mentioned one-step iterative methods are even susceptible to noise because they lack the ability to suppress noise or require manual adjustment of the parameters of the regularization terms when the number of materials increases. Direct extensions and applications of these methods to multi-material reconstructions are unstable and may even fail due to the increased ill-posedness arising from inconsistent geometry. Therefore, it is a key issue to design an efficient and accurate one-step method based on an appropriate optimization model for multi-material imaging in spectral CT.

In this work, for multi-material reconstruction under inconsistent geometry, a statistical reconstruction model is established that combines different material-specific image regularization priors. When the number of spectrums matches the number of materials, a gradient sparsity TV based prior and a denoising convolutional neural network (DnCNN) [34] based prior are incorporated into the statistical model. For the case where the number of spectrums does not match the number of materials, a volume conservation constraint (VCC) is developed to improve the ill-condition of the inverse problem. Additionally, an efficient Newton descent algorithm is derived based on the simple surrogate function. To verify the practical performance of the presented methods, a series of numerical experiments have been conducted, which show that the proposed algorithms demonstrate improved results of noise suppression compared to the state-of-the-art one-step material reconstruction methods.

The organization of this paper is as follows. Section II introduces the physical model, and describes the proposed reconstruction algorithms. Section III presents the numerical verifications of the proposed methods and experimental comparisons with typical competing methods. Discussions and conclusions are subsequently presented in Section IV and Section V, respectively.

II. MATERIALS AND METHODS

A. STATISTICAL MULTI-MATERIAL RECONSTRUCTION MODEL

Spectral CT is a promising imaging technique that takes advantage of the differences in attenuation of different materials in an object when polychromatic X-ray passes through

it. Specifically, the attenuation of an object $\boldsymbol{f}(x, E)$ at a particular ray l under a specific spectrum $S_s(E)$ follows the formula:

$$y_{s,l} = \int S_s(E) \exp(-\int_l \boldsymbol{f}(x, E) dl) dE, \tag{1}$$

where $l \in \Omega_s, s = 1, 2, \ldots, S$. Furthermore, $\boldsymbol{f}(x, E)$ can be decoupled into a linear combination of energy-dependent terms $\mu_k(E)$ and basis material-dependent terms $\boldsymbol{f}_k(x)$, i.e.,

$$\boldsymbol{f}(x, E) = \sum_{k=1}^{K} \mu_k(E) \boldsymbol{f}_k(x), \tag{2}$$

where K is the total number of basis materials. In general, the discrete form is utilized to establish the forward transmission model:

$$y_{s,l} = \sum_{m=1}^{M_s} S_{s,m} \exp(-\sum_{k=1}^{K} \mu_{m,k} A_{s,l} \boldsymbol{f}_k), \tag{3}$$

where $S_{s,m}$ is the sampling point of the energy spectrum $S_s(E)$, and $\sum_{m=1}^{M_s} S_{s,m} = 1$. $A_{s,l}$ represents the line integral of basis material $\boldsymbol{f}_k$ and the path of the ray l. For spectral CT imaging, the measurements is assumed to follow the Poisson model:

$$y_{s,l} \sim Poisson(\sum_{m=1}^{M_s} S_{s,m} \exp(-\sum_{k=1}^{K} \mu_{m,k} A_{s,l} \boldsymbol{f}_k)), \tag{4}$$

For the inconsistent scanning geometry, the path of the measured ray under one spectrum does not coincide with another spectrum. In other words, the intersection of any two sets of the ray l is empty ($\Omega_{s1} \cap \Omega_{s2} = \emptyset$, $s1, s2 \in \{1, \ldots, S\}$). Assuming that the expected photons $y_{s,l}$ follow a Poisson statistical model. Given the measurements $\hat{y}$, the negative log-likelihood function with respect to the expected photons is

$$\begin{aligned} L(\boldsymbol{f}_1, \boldsymbol{f}_2, \cdots \boldsymbol{f}_K) = & \sum_{s,l} y_{s,l}(\boldsymbol{f}_1, \boldsymbol{f}_2, \cdots \boldsymbol{f}_K) \\ & - \hat{y}_{s,l} \ln y_{s,l}(\boldsymbol{f}_1, \boldsymbol{f}_2, \cdots \boldsymbol{f}_K). \end{aligned} \tag{5}$$

However, minimizing the negative log-likelihood function for the polychromatic measurements is always ill-posed due to severe noise. It needs to combine it with some prior knowledge as a regularization term to improve the condition of the solution. Therefore, the multi-material reconstruction model is described as

$$\min_{\boldsymbol{f}_1, \boldsymbol{f}_2, \cdots \boldsymbol{f}_K} L(\boldsymbol{f}_1, \boldsymbol{f}_2, \cdots \boldsymbol{f}_K) + \lambda R(\boldsymbol{f}_1, \boldsymbol{f}_2, \cdots \boldsymbol{f}_K) \tag{6}$$

where $R(\boldsymbol{f}_1, \boldsymbol{f}_2, \cdots \boldsymbol{f}_K)$ is the mathematical symbolic representation of prior knowledge, such as gradient sparsity of reconstructed images and other material-specific knowledge. λ is a scaling nonnegative factor that balances the regularization term.

B. PRIORS BASED METHODS FOR INCONSISTENT POLYCHROMATIC PROJECTION

From the definition of $L(\boldsymbol{f}_1, \boldsymbol{f}_2, \cdots \boldsymbol{f}_K)$, there are the operations of summing first and then taking the logarithm. It is challenging to obtain the analytical solution directly. One intuitive approach is to find a simpler representation of the complex function that is easier to solve. In order to achieve this, we first rewrite equation (5) as

$$\begin{aligned} & L(\boldsymbol{f}_1, \boldsymbol{f}_2, \cdots \boldsymbol{f}_K) \\ & = \sum_{s,l} y_{s,l}(\boldsymbol{f}_1, \boldsymbol{f}_2, \cdots \boldsymbol{f}_K) \\ & \quad - \hat{y}_{s,l} \ln y_{s,l}(\boldsymbol{f}_1, \boldsymbol{f}_2, \cdots \boldsymbol{f}_K) \\ & = \sum_{s,l} \sum_{m=1}^{M_s} S_{s,m} \exp(-\sum_{k=1}^{K} \mu_{m,k} A_{s,l} \boldsymbol{f}_k) \\ & \quad - \hat{y}_{s,l} \ln \sum_{m=1}^{M_s} S_{s,m} \exp(-\sum_{k=1}^{K} \mu_{m,k} A_{s,l} \boldsymbol{f}_k) \\ & = \sum_{s,l} \sum_{m=1}^{M_s} \frac{S_{s,m}}{\alpha^{(n)}} \alpha^{(n)} t(\boldsymbol{f}_1, \boldsymbol{f}_2, \cdots \boldsymbol{f}_K) \\ & \quad - \hat{y}_{s,l} \ln \sum_{m=1}^{M_s} \frac{S_{s,m}}{\alpha^{(n)}} \alpha^{(n)} t(\boldsymbol{f}_1, \boldsymbol{f}_2, \cdots \boldsymbol{f}_K), \end{aligned} \tag{7}$$

where $t(\boldsymbol{f}_1, \boldsymbol{f}_2, \cdots \boldsymbol{f}_K) = \exp(-\sum_{k=1}^{K} \mu_{m,k} A_{s,l} \boldsymbol{f}_k)$, and $\alpha^{(n)}$ is a nonnegative parameter. To obtain a more explicit expression for the parameter $\alpha^{(n)}$, it is necessary to state that $\alpha^{(n)}$ satisfies the assumption $\sum_{m=1}^{M_s} \alpha^{(n)} = \sum_{m=1}^{M_s} \alpha(\boldsymbol{f}_1^{(n)}, \ldots, \boldsymbol{f}_K^{(n)}) = 1$. When combined with the fact that $h(x) = x - y \ln x$ is a convex function, the above equation (7) can be transformed into finding its upper bound by Jensen's inequality

$$\begin{aligned} L(\boldsymbol{f}_1, \boldsymbol{f}_2, \cdots \boldsymbol{f}_K) = & \sum_{s,l} \sum_{m=1}^{M_s} \frac{S_{s,m}}{\alpha^{(n)}} \alpha^{(n)} t(\boldsymbol{f}_1, \boldsymbol{f}_2, \cdots \boldsymbol{f}_K) \\ & - \hat{y}_{s,l} \ln \sum_{m=1}^{M_s} \frac{S_{s,m}}{\alpha^{(n)}} \alpha^{(n)} t(\boldsymbol{f}_1, \boldsymbol{f}_2, \cdots \boldsymbol{f}_K) \\ \leq & \sum_{s,l} \sum_{m=1}^{M_s} \alpha^{(n)} [\frac{S_{s,m}}{\alpha^{(n)}} t(\boldsymbol{f}_1, \boldsymbol{f}_2, \cdots \boldsymbol{f}_K) \\ & - \hat{y}_{s,l} \ln \frac{S_{s,m}}{\alpha^{(n)}} t(\boldsymbol{f}_1, \boldsymbol{f}_2, \cdots \boldsymbol{f}_K)]. \end{aligned} \tag{8}$$

If the equality holds, the upper bound is close to the original objective function $L(\boldsymbol{f}_1, \boldsymbol{f}_2, \cdots \boldsymbol{f}_K)$. Therefore, we need to construct a proper $\alpha^{(n)}$ to make the equality hold, i.e., the equality holds if and only if the value is a constant. Hence, the following equation at the point $(\boldsymbol{f}_1^{(n)}, \ldots, \boldsymbol{f}_K^{(n)})$ is established

$$\frac{S_{s,m}}{\alpha^{(n)}} t(\boldsymbol{f}_1^{(n)}, \ldots, \boldsymbol{f}_K^{(n)}) = c, \tag{9}$$

where c is a constant. According to $\sum_{m=1}^{M_s} \alpha^{(n)} = 1$, we get the explicit formula of $\alpha^{(n)}$ as

$$\alpha^{(n)} = \frac{S_{s,m} t(\boldsymbol{f}_1^{(n)}, \ldots, \boldsymbol{f}_K^{(n)})}{\sum_{m=1}^{M_s} S_{s,m} t(\boldsymbol{f}_1^{(n)}, \ldots, \boldsymbol{f}_K^{(n)})} = \frac{S_{s,m} t^{(n)}}{\sum_{m=1}^{M_s} S_{s,m} t^{(n)}} = \frac{S_{s,m} t^{(n)}}{y_{s,l}^{(n)}}. \tag{10}$$

We further denote $\beta^{(n)} = \frac{S_{s,m}}{\alpha^{(n)}} = \frac{y_{s,l}^{(n)}}{t^{(n)}}$, then $\alpha^{(n)} = \frac{S_{s,m}}{\beta^{(n)}}$ and

$$\begin{aligned} L(\boldsymbol{f}_1, \boldsymbol{f}_2, \cdots \boldsymbol{f}_K) &\le \sum_{s,l} \sum_{m=1}^{M_s} \alpha^{(n)} [\frac{S_{s,m}}{\alpha^{(n)}} t(\boldsymbol{f}_1, \boldsymbol{f}_2, \cdots \boldsymbol{f}_K) \\ &\quad - \hat{y}_{s,l} \ln \frac{S_{s,m}}{\alpha^{(n)}} t(\boldsymbol{f}_1, \boldsymbol{f}_2, \cdots \boldsymbol{f}_K)] \\ &= \sum_{s,l} \sum_{m=1}^{M_s} \frac{S_{s,m}}{\beta^{(n)}} (\beta^{(n)} t(\boldsymbol{f}_1, \boldsymbol{f}_2, \cdots \boldsymbol{f}_K) \\ &\quad - \hat{y}_{s,l} \ln \beta^{(n)} t(\boldsymbol{f}_1, \boldsymbol{f}_2, \cdots \boldsymbol{f}_K)) \\ &= \sum_{m=1}^{M_s} S_{s,m} \sum_{s,l} \frac{1}{\beta^{(n)}} (\beta^{(n)} t(\boldsymbol{f}_1, \boldsymbol{f}_2, \cdots \boldsymbol{f}_K) \\ &\quad - \hat{y}_{s,l} \ln \beta^{(n)} t(\boldsymbol{f}_1, \boldsymbol{f}_2, \cdots \boldsymbol{f}_K)) \\ &= \sum_{m=1}^{M_s} S_{s,m} \hat{L}(\boldsymbol{f}_1, \boldsymbol{f}_2, \cdots \boldsymbol{f}_K) \end{aligned} \tag{11}$$

where

$$\begin{aligned} \hat{L}(\boldsymbol{f}_1, \boldsymbol{f}_2, \cdots \boldsymbol{f}_K) = \sum_{s,l} \frac{1}{\beta^{(n)}} (\beta^{(n)} t(\boldsymbol{f}_1, \boldsymbol{f}_2, \cdots \boldsymbol{f}_K) \\ - \hat{y}_{s,l} \ln \beta^{(n)} t(\boldsymbol{f}_1, \boldsymbol{f}_2, \cdots \boldsymbol{f}_K)). \end{aligned}$$

and $\sum_{m=1}^{M_s} S_{s,m} \hat{L}(\boldsymbol{f}_1, \boldsymbol{f}_2, \cdots \boldsymbol{f}_K)$ is the desired final representation mentioned at the beginning of the subsection. Although the original objective function $L(\boldsymbol{f}_1, \boldsymbol{f}_2, \cdots \boldsymbol{f}_K)$ is approximated, the simple function is equivalent to $L(\boldsymbol{f}_1, \boldsymbol{f}_2, \cdots \boldsymbol{f}_K)$ at a certain point in the construction process.

Algorithm 1 TV-Based Method

Input: measured projection data $\hat{y}_{s,l}$, parameter λ, $n_{\max}$.
Initialization: $\boldsymbol{f}_k^{(0)} (k = 1, 2, \ldots, K)$, $n = 0$.
While $n \le n_{\max}$
  Update $\boldsymbol{f}_k^{(n)} (k = 1, 2, \ldots, K)$ via (14).
End while
Output: $\boldsymbol{f}_k, (k = 1, \ldots, K)$

C. GRADIENT SPARSITY-BASED ALGORITHM

In this subsection, TV is utilized to characterize the material maps sparsity, i.e., the regularization term $R(\boldsymbol{f}_1, \boldsymbol{f}_2, \cdots \boldsymbol{f}_K) = \sum_{k=1}^{K} \left\| \nabla \boldsymbol{f}_k \right\|_1$, where $\nabla \boldsymbol{f}_k := (\nabla_x \boldsymbol{f}_k, \nabla_y \boldsymbol{f}_k)$ denotes differential operator along the x and y directions. And the TV term is defined as

$$\left\| \nabla \boldsymbol{f}_k \right\|_1 = \left\| \nabla_x \boldsymbol{f}_k \right\|_1 + \left\| \nabla_y \boldsymbol{f}_k \right\|_1. \tag{12}$$

Therefore, the gradient sparsity based reconstruction model can be illustrated as

$$\min_{\boldsymbol{f}_1, \boldsymbol{f}_2, \cdots \boldsymbol{f}_K} \sum_{m=1}^{M_s} S_{s,m} \hat{L}(\boldsymbol{f}_1, \boldsymbol{f}_2, \cdots \boldsymbol{f}_K) + \lambda \sum_{k=1}^{K} \left\| \nabla \boldsymbol{f}_k \right\|_1 \tag{13}$$

To solve the optimization problem, the Newton method is applied to get new iterations in equation (14), as shown at the bottom of the page, where $diag(x)$ denotes the diagonal matrix of x. Note that the continuous function $\|\cdot\|_1$ is not differentiable, but for a discrete digital two-dimensional image, the symbols of the first and second derivatives here represent operations pixel-wised. The overall description of the gradient sparsity based method is summarized in Algorithm 1.

D. DEEP PRIOR-BASED ALGORITHM

Rather than the TV penalty, we also consider a deep prior, DnCNN, as a flexible module under the plug-and-play (PnP) framework [35]. The deep prior-based multi-material reconstruction model is

$$\min_{\boldsymbol{f}_1, \boldsymbol{f}_2, \cdots \boldsymbol{f}_K} \sum_{m=1}^{M_s} S_{s,m} \hat{L}(\boldsymbol{f}_1, \boldsymbol{f}_2, \cdots \boldsymbol{f}_K) + \lambda \sum_{k=1}^{K} \Phi(\boldsymbol{f}_k) \tag{15}$$

$$\begin{aligned} \boldsymbol{f}_k^{(n+1)} &= \boldsymbol{f}_k^{(n)} - \Delta \boldsymbol{f}_k^{(n)} \\ &= \boldsymbol{f}_k^{(n)} - \sum_k \frac{(\sum_{m=1}^{M_k} S_{s,m} \frac{\partial \hat{L}(\boldsymbol{f}_1, \boldsymbol{f}_2, \cdots \boldsymbol{f}_K)}{\boldsymbol{f}_k} + \lambda \frac{\partial \sum_{k=1}^{K} \left\| \nabla \boldsymbol{f}_k \right\|_1}{\boldsymbol{f}_k}) \Big|_{\boldsymbol{f}_k = \boldsymbol{f}_k^{(n)}}}{(\frac{\partial^2 \hat{L}(\boldsymbol{f}_1, \boldsymbol{f}_2, \cdots \boldsymbol{f}_K)}{\partial \boldsymbol{f}_k^2} + \frac{\partial^2 \sum_{k=1}^{K} \left\| \nabla \boldsymbol{f}_k \right\|_1}{\partial \boldsymbol{f}_k^2}) \Big|_{\boldsymbol{f}_k = \boldsymbol{f}_k^{(n)}}} \\ &= \boldsymbol{f}_k^{(n)} - \sum_k \frac{\sum_{s,l} A_{s,l}^T \cdot (\frac{\hat{y}_{s,l}}{y_{s,l}^{(n)}} - 1) \sum_{m=1}^{M_k} S_{s,m} \mu_{m,k} t^{(n)} + \lambda \nabla^T \left\| \nabla \boldsymbol{f}_k \right\|_1 \Big|_{\boldsymbol{f}_k = \boldsymbol{f}_k^{(n)}}}{\sum_{s,l} A_{s,l}^T \cdot A_{s,l} \cdot \sum_{m=1}^{M_k} S_{s,m} \mu_{m,k}^2 t^{(n)} + diag(\nabla^T \nabla)}, \quad (k = 1, 2, \ldots, K), \end{aligned} \tag{14}$$

where $\Phi(\boldsymbol{f}_k)$ is the DnCNN deep prior in terms of k-th basis material. Furthermore, auxiliary variables $\boldsymbol{g}_1, \boldsymbol{g}_2, \cdots \boldsymbol{g}_K$ are introduced to transform the problem as

$$\min_{\boldsymbol{f}_k, \boldsymbol{g}_k} \sum_{m=1}^{M_s} S_{s,m}\hat{L}(\boldsymbol{f}_1, \boldsymbol{f}_2, \cdots \boldsymbol{f}_K) + \lambda \sum_{k=1}^{K} \Phi(\boldsymbol{g}_k) + \sum_{k=1}^{K} \frac{\lambda_k}{2} \left\| \boldsymbol{f}_k - \boldsymbol{g}_k + \frac{\Lambda_k}{\lambda_k} \right\|_2^2, \quad k = 1, \ldots, K, \tag{16}$$

where Λ_k is the Lagrangian multiplier, and λ_k is the nonnegative penalty parameter. The alternating directions method of multipliers (ADMM) is adopted to solve the problem (16), it is divided into two sub-problems (17) and (18), as shown at the bottom of the page.

The implementation of sub-problems $\boldsymbol{g}_1, \boldsymbol{g}_2, \cdots \boldsymbol{g}_K$ is a denoising process based on a pre-trained DnCNN network. Feeding $\boldsymbol{f}_k^{(n+1)} + \frac{\Lambda_k^{(n)}}{\lambda_k}$ into the denoiser DnCNN network, we obtain the solution $\boldsymbol{g}_k^{(n+1)}$. The parameter $\sqrt{\lambda/\lambda_k}$ is related to the error estimation between the clean and noisy images. The summary of the deep prior-based material reconstruction (DnCNN-based) method is listed in Algorithm 2.

Algorithm 2 DnCNN-Based Method

Input: measured projection data $\hat{y}_{s,l}$, parameter $\lambda, n_{\max}, \lambda_k (k = 1, \ldots, K)$.
Initialization: $\boldsymbol{f}_k^{(0)}, \boldsymbol{g}_k^{(0)} (k = 1, 2, \ldots, K), n = 0$.
While $n \leq n_{\max}$
For $k = 1, 2, \ldots, K$
1. Update $\boldsymbol{f}_k^{(n)}$ via (17).
2. Update $\boldsymbol{g}_k^{(n)}$ via (18).
3. $\Lambda_k^{(n+1)} = \Lambda_k^{(n)} + \lambda_k(\boldsymbol{f}_k^{(n+1)} - \boldsymbol{g}_k^{(n+1)})$.
End while
Output: $\boldsymbol{f}_k, (k = 1, \ldots, K)$

E. VOLUME CONSERVATION CONSTRAINT-BASED ALGORITHM

If the numbers of the basis materials and spectrums are not the same, i.e., the known spectrums are less than the number of materials, the nonlinear inverse problem can be described as

$$\begin{cases} y_{1,l} = \sum_{m=1}^{M_1} S_{1,m} \exp(-\sum_{k=1}^{K} \mu_{m,k} A_{1,l} \boldsymbol{f}_k), \\ y_{2,l} = \sum_{m=1}^{M_2} S_{1,m} \exp(-\sum_{k=1}^{K} \mu_{m,k} A_{2,l} \boldsymbol{f}_k), \\ \cdots \\ y_{s-1,l} = \sum_{m=1}^{M_{s-1}} S_{s-1,m} \exp(-\sum_{k=1}^{K} \mu_{m,k} A_{s-1,l} \boldsymbol{f}_k). \end{cases}$$

It means that the nonlinear equation system about the unknown basis materials $\boldsymbol{f}_k, k = 1, 2, \ldots, K$ is more ill-posed and the existence of noise will aggravate the difficulty of solving the inverse problem. Similar to the previous two subsections, the intuitive idea is to introduce regularization terms to suppress the adverse effects of noise. In addition, we further assume that the volume of basis materials in a voxel or pixel is conserved. Under this assumption, the volume conservation constraint is proposed to reduce the difficulty through adding nonlinear equations, which formulation is derived as (20). Therefore, the minimization is reformulated as

$$\min_{\boldsymbol{f}_1, \boldsymbol{f}_2, \cdots \boldsymbol{f}_K} \sum_{m=1}^{M_s} S_{s,m}\hat{L}(\boldsymbol{f}_1, \boldsymbol{f}_2, \cdots \boldsymbol{f}_K) + \lambda \sum_{k=1}^{K} \|\nabla \boldsymbol{f}_k\|_1 \quad s.t. \sum_{k=1}^{K} \boldsymbol{f}_k = T_0, \tag{19}$$

where T_0 is a template and its pixel is 1 when the material is present. We try to integrate this equality constraint in the descent step of basis materials. First, we convert the constraint into projection data at an auxiliary normalized

$$\begin{aligned} \boldsymbol{f}_k^{(n+1)} &= \arg\min_{\boldsymbol{f}_k} \sum_{m=1}^{M_s} S_{s,m}\hat{L}(\boldsymbol{f}_1, \boldsymbol{f}_2, \cdots \boldsymbol{f}_K) + \sum_{k=1}^{K} \frac{\lambda_k}{2} \left\| \boldsymbol{f}_k - \boldsymbol{g}_k^{(n)} + \frac{\Lambda_k^{(n)}}{\lambda_k} \right\|_2^2 \\ &= \boldsymbol{f}_k^{(n)} - \sum_k \frac{\sum_{s,l} A_{s,l}^T \cdot (\frac{\hat{y}_{s,l}}{y_{s,l}^{(n)}} - 1) \sum_{m=1}^{M_k} S_{s,m}\mu_{m,k} t^{(n)} + \lambda_k (\boldsymbol{f}_k - \boldsymbol{g}_k^{(n)} + \frac{\Lambda_k^{(n)}}{\lambda_k}) \big|_{\boldsymbol{f}_k = \boldsymbol{f}_k^{(n)}}}{\sum_{s,l} A_{s,l}^T \cdot A_{s,l} \cdot \sum_{m=1}^{M_k} S_{s,m}\mu_{m,k}^2 t^{(n)} + \lambda_k}, \quad k = 1, \ldots, K, \end{aligned} \tag{17}$$

$$\begin{aligned} \boldsymbol{g}_k^{(n+1)} &= \arg\min_{\boldsymbol{g}_k} \sum_{k=1}^{K} \Phi(\boldsymbol{g}_k) + \sum_{k=1}^{K} \frac{1}{2\lambda/\lambda_k} \left\| \boldsymbol{f}_k^{(n+1)} - \boldsymbol{g}_k + \frac{\Lambda_k^{(n)}}{\lambda_k} \right\|_2^2 \\ &= DnCNN(\boldsymbol{f}_k^{(n+1)} + \frac{\Lambda_k^{(n)}}{\lambda_k}, \sqrt{\lambda/\lambda_k}), \quad k = 1, \ldots, K. \end{aligned} \tag{18}$$

spectrum S_T, i.e.,

$$y_{T_0,l} = \sum_{m=1}^{M_T} S_{T,m} \exp(-\sum_{k=1}^{K} A_{T,l} \boldsymbol{f}_k), \quad y_{T_0} = \sum_l y_{T_0,l}, \tag{20}$$

where $A_{T,l}$ denotes the path of l-th ray under the scanning geometry, M_T is the total number of sampling at the current energy. $\sum_{m=1}^{M_T} S_{T,m} = 1$ and it should be pointed out that $S_{T,m}$ of the auxiliary spectrum can be equal to $1/M_T$. We further get a pre-computed $\hat{y}_{T_0,l} = \sum_{m=1}^{M_T} S_{T,m} \exp(-A_{T,l} T_0)$. Then, similar to the construction of $\beta^{(n)}$, $t^{(n)}$, we obtain

$$\begin{aligned} t_{T_0}(\boldsymbol{f}_1, \boldsymbol{f}_2, \cdots \boldsymbol{f}_K) &= \exp(-\sum_{k=1}^{M_T} A_{T,l} \boldsymbol{f}_k), \beta_{T_0}^{(n)} \\ &= \frac{y_{T_0,l}(\boldsymbol{f}_1^{(n)}, \boldsymbol{f}_2^{(n)}, \cdots \boldsymbol{f}_K^{(n)})}{t_{T_0}(\boldsymbol{f}_1^{(n)}, \boldsymbol{f}_2^{(n)}, \cdots \boldsymbol{f}_K^{(n)})} = \frac{y_{T_0,l}^{(n)}}{t_{T_0}^{(n)}}. \end{aligned} \tag{21}$$

Finally, we establish the surrogate function of y_{T_0},

$$\begin{aligned} Ly_{T_0} &= \sum_l y_{T_0,l} - \hat{y}_{T_0,l} \ln y_{T_0,l} \\ &\le \sum_l \sum_{m=1}^{M_T} \frac{S_{T,m}}{\beta_{T_0}^{(n)}} (\beta_{T_0}^{(n)} t_{T_0} - \hat{y}_{T_0,l} \ln \beta_{T_0}^{(n)} t_{T_0}) \\ &= \sum_{m=1}^{M_T} S_{T,m} \sum_l \frac{1}{\beta_{T_0}^{(n)}} (\beta_{T_0}^{(n)} t_{T_0} - \hat{y}_{T_0,l} \ln \beta_{T_0}^{(n)} t_{T_0}) \\ &= \sum_{m=1}^{M_T} S_{T,m} \hat{L} y_{T_0}(\boldsymbol{f}_1, \boldsymbol{f}_2, \cdots \boldsymbol{f}_K). \end{aligned} \tag{22}$$

And other derivations are similar to the previous descriptions. Similar to the previous update, Newton's method is applied to obtain the iterative form of the main formula as well while the regularization term is chosen as TV penalty as (23), shown at the bottom of the page.

The overall description of the volume conservation constraint based method is summarized in Algorithm 3.

Algorithm 3 VCC-Based Method

Input: measured projection data $\hat{y}_{s,l}$, parameter λ, $n_{\max}$.
Initialization: $\boldsymbol{f}_k^{(0)} (k = 1, 2, \ldots, K)$, $n = 0$.
While $n \le n_{\max}$
  Update $\boldsymbol{f}_k^{(n)} (k = 1, 2, \ldots, K)$ via (19).
End while
Output: $\boldsymbol{f}_k, (k = 1, \ldots, K)$

III. RESULTS

In this section, the performance of the proposed method will be validated through a simulated walnut data [36] and an industrial QRM phantom dataset. The comparison methods are chosen as the three-material EART, the three-material OPMT, the TV-based method listed in Algorithm 1, the DnCNN-based method listed in Algorithm 2, and the VCC-based method listed in Algorithm 3. To further clarify the effectiveness of the proposed algorithms, the root mean square error (RMSE), the peak signal-to-noise ratio (PSNR), and the structural similarity index (SSIM) [37] are employed for quantitative assessment. In addition, to accelerate the algorithms, the ordered subsets (OS) technique [38] is adopted to implement experiments, and the OS number is set to 33 for our proposed methods in the numerical experiments. In the simulation experiments, the regularized penalty parameters λ of proposed methods are set to 1. And in the real dataset, the corresponding λ of the proposed methods are set to 10^{-2}, 1, and 10^{-3}, respectively. The parameters of comparison methods are also modified according to the condition of different datasets. And the total number of iterations are set to 3000 and 30 for noisy simulation and real experiments, respectively.

A. SIMULATION EXPERIMENTS

The simulated walnut dataset with the size of 512×512 pixels contains three materials, i.e., tissue, bone, and iodine, which is shown in Figure 1(a1)-(a4). And the concentration of the iodine contrast agent is 15 mg/mL. The attenuation curves of three materials are shown in Figure 1(b). The distances of source-to-object and source-to-detector are 300.0 mm and 600.0 mm. The three source spectrums for the simulation data are generated by the SpekCalc software [39] at 80 kVp, 110 kVp, and 140 kVp, the distributions are shown in Figure 1(c). Projections of each spectrum are acquired from 363 views uniformly distributed in the 360° range under a fan beam scanning geometry. And the number of detector units is 1024 with the size of 0.124 mm. The ray paths of three

$$\boldsymbol{f}_k^{(n+1)} = \boldsymbol{f}_k^{(n)} - \Delta \boldsymbol{f}_k^{(n)} = \boldsymbol{f}_k^{(n)} - \frac{\sum_{s,l} A_{s,l}^T \cdot (\frac{\hat{y}_{s,l}}{y_{s,l}^{(n)}} - 1) \sum_{m=1}^{M_k} S_{s,m} \mu_{m,k} t^{(n)} + \sum_l A_{s,l}^T \cdot (\hat{y}_{T_0,l} - y_{T_0,l}^{(n)}) + \lambda \nabla^T \left\| \nabla \boldsymbol{f}_k \right\|_1 \Big|_{\boldsymbol{f}_k = \boldsymbol{f}_k^{(n)}}}{\sum_{s,l} A_{s,l}^T \cdot A_{s,l} \cdot \sum_{m=1}^{M_k} S_{s,m} \mu_{m,k}^2 t^{(n)} + \sum_l A_{s,l}^T \cdot A_{s,l} \cdot y_{T_0,l}^{(n)} + diag(\nabla^T \nabla) \Big|_{\boldsymbol{f}_k = \boldsymbol{f}_k^{(n)}}}, \quad (k = 1, 2, \ldots, K). \tag{23}$$

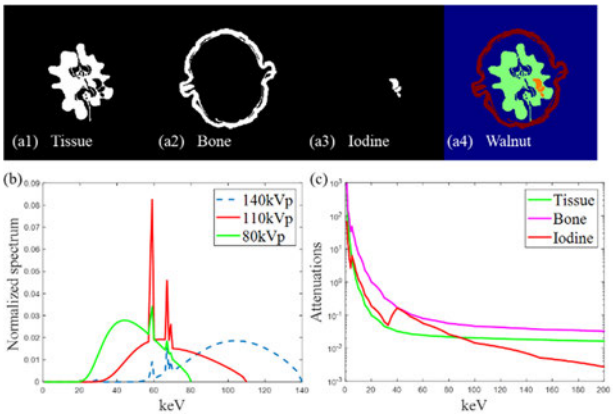

FIGURE 1. (a) Simulation walnut phantom that consists of (a1) tissue, (a2) bone, and (a3) iodine, and (a4) represents the simulated object. (b) Three normalized spectrums were used in the simulation experiments. (c) Linear attenuations of different materials.

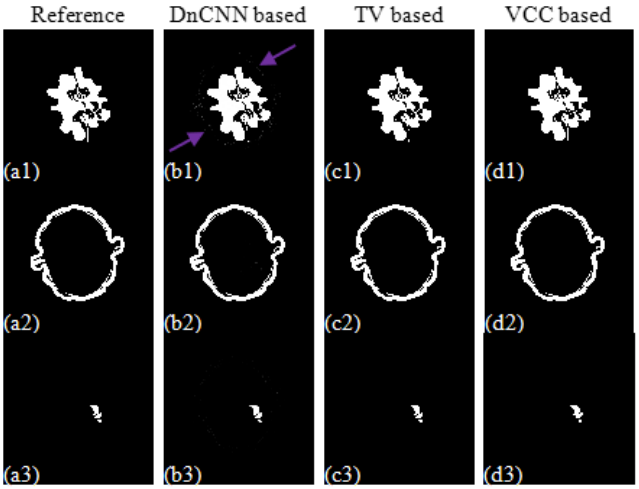

FIGURE 2. Results of noise-free simulation dataset obtained by the proposed methods. Columns (a) to (d) represent the Reference, the TV-based method, the DnCNN-based method, and the VCC-based method, respectively. Rows from top to bottom indicate three materials: tissue, bone, and iodine, respectively, where the display windows of the first two columns are [0.02 1], [0.01 1], and [0.01 1], respectively.

spectrums are inconsistent to obtain the measured projections in the fast kVp switching scanning. In the experiments, the initial images for all methods are set to zero, and the spectrums used in the VCC-based method are the high and low voltages, i.e., 80 kVp and 140 kVp.

B. NOISE-FREE DATA VERIFICATION

In this subsection, the ideal noise-free walnut data are first applied to verify the performance of the proposed methods. Figure 2 shows the materials maps reconstructed by the proposed method, where columns (a) to (d) represent the ground truth (Reference), the TV-based method, the DnCNN-based method, and the VCC-based method, respectively. Rows from up to bottom are the distributions of tissue, bone, and iodine materials. According to the results shown in Figure 2, the material maps reconstructed by the proposed methods are close to the given phantom maps in most areas. Since DnCNN is a pre-trained network, it is easy to overfit when the number of iterations is too large. This is also shown by the results reconstructed by the DnCNN-based method. For example, it shows some bone structures in the tissue map, as shown by purple arrows in Figure 2 (b1). We further plot the RMSE curves of different materials for the three proposed methods.

As shown in Figure 3(a), the proposed VCC-based method has a faster descent trend compared with the TV-based method and the DnCNN-based method. The reason for this phenomenon is that the former only utilizes two spectrums to update, while the latter requires three energies to acquire three material maps. Meanwhile, DnCNN based method has an upward trend with the increase of iteration due to the overfitting. In addition, three different forms of the volume conservation constraint are tested.

In Figure 3(b), the high spectrum represents the high energy (140 kVp) used in the simulation experiments. The equal spectrum means that the normalized spectrum used in the VCC-based method is discretized into 140 sampling points, and the intensity of every point is equal. And 2-equal spectrum indicates that we computed two volume conservation constraints in the implementation with two equal spectrums at 140 sampling points and 80 sampling points. The results of RMSEs show that the high spectrum and equal spectrum have the same positive effect on the algorithm. Their curves overlap in Figure 3(b). And the 2-equal spectrum also declined, and at a faster rate than the other two tested spectrums. The reason for this phenomenon is that the two equality constraints at two spectrums are enforced to accelerate the convergence. From these results, it demonstrates that the introduction of the volume conservation constraint in the VCC-based method plays an important role in multi-material reconstruction and it does not require additional estimation of the spectrum. Note that the results of the VCC-based method were obtained by the usage of two equality constraints.

C. COMPARISON EXPERIMENTS WITH NOISY DATA

In this subsection, comparisons with the state-of-art algorithms will be carried out to further verify the performance of the proposed method. To make the data more realistic, different Poisson noise levels are added to obtained projections to simulate image noises. In this work, Poisson noise is generated and injected into the projections to simulate noisy measurements as

$$P = \frac{I_0^k}{k!} e^{-I_0}, \quad \boldsymbol{p}_i = P \cdot \exp(-\boldsymbol{p}_0), \tag{24}$$

where I_0 stands for the number of incident X-ray photons, $\boldsymbol{p}_0, \boldsymbol{p}$ are the measured projection data and the photons of adding noise collected by the detector unit i, respectively. k is the index of the detector unit. In this work, we set $I_0 = 1e5$ and $I_0 = 1e7$ to validate the effectiveness of the proposed algorithm.

Figure 4 and Figure 5 show the materials results, virtual monochromatic images at 75 keV reconstructed by different

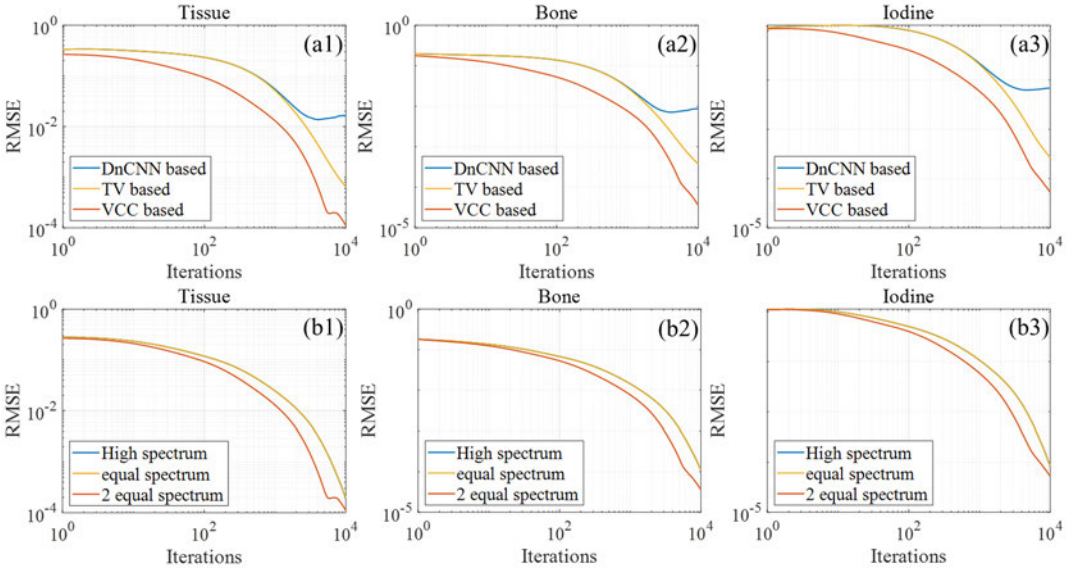

FIGURE 3. (a) The RMSE curves of the proposed three methods, (b) The verified RMSE curves of different spectrums used in the VCC-based method. Columns from left to right represent tissue, bone, and iodine materials.

methods at two different noise levels, and the corresponding difference images, where the columns (a) to (f) represent the images of Reference, EART, OPMT, TV-based method, DnCNN-based method, and VCC-based method, respectively. Compared with the Reference, the results of the EART method are relatively inaccurate, especially in the imaging of tissue, there are still parts of the bone in tissue images. And the difference images obtained by EART are comparatively noisy, indicated by the purple arrow in Figure 4 (b5). The results of the OPMT method have a considerable improvement. But at the high noise level, the tissue map of OPMT has obvious noise due to the lack of noise suppression capability, especially in the area marked by the purple arrow in Figure 5 (c4) and (c5). Compared with EART and OPMT methods, the three prior-based methods have the ability to suppress noise, which has been indicated in the reconstructed material maps. In particular, there are some misclassifications in the tissue and iodine basis materials of the DnCNN-based method. The reason is that the DnCNN method is derived under the ADMM framework and its decreasing trend is slower than that of the Newton method with the same iterations. Furthermore, the last rows of Figure 4 and Figure 5 demonstrate the virtual monochromatic images of different methods. The results show that the proposed methods have the ability to suppress noise when compared with the EART and OPMT algorithms.

Quantitative evaluations are listed in Table 1. Taking the high noise level $I_0 = 1e5$ as an example to illustrate the overall performance of different methods. It can be seen from Table 1 that the averaged PSNRs for three materials of the proposed three algorithms are 32.951 dB, 42.009 dB, and 47.173 dB, respectively. And the highest value is obtained by the VCC-based method, which increased PSNRs by 20.924 dB and 18.283 dB compared with those of the EART and OPMT methods, respectively. And the averaged SSIMs for the proposed three algorithms are all over 0.94, where the VCC-based method obtains the highest SSIM index of 0.999, while the SSIMs of EART and OPMT are below 0.94. In addition, the highest averaged RMSE among the three proposed algorithms is 0.00592, which reduced RMSEs by 89.65% and 88.79% compared with those of the EART and OPMT methods. The line profiles of different materials, drawn from the pixels along the white dashed line in Fig. 4 (a1) and Fig.5 (a1), are further plotted in Fig.6. It demonstrates that the TV-based method and VCC-based method obtain more accurate structures and details than EART and OPME methods, especially in the areas pointed by the purple arrows.

D. REAL QRM DATA EXPERIMENT

In this section, the performance of the proposed methods is investigated by an industrial QRM phantom, which consists of five different materials including cortical mandible bone, spongious bone, muscle, CT water, and adipose. The diameters of the phantom and each cylinder are 100.0 mm and 20.0 mm, respectively. It should be pointed out that two different densities of bone are considered to the bone basis material, CT water and adipose have seemed as water basis material with impurities, which is shown in Figure 7.

The QRM phantom data is obtained using an industrial CT system in our laboratory under a cone beam system, which mainly composes of an X-ray rotary stage with an object holder and flat panel detector (4030E, Varian, USA). The QRM is scanned repeatedly at tube voltages 60, 80, and 100 kVp along a circular line and the tube current is set to 220 μA for every scanning. The central slice of each two-dimensional projection is extracted and down-sampled

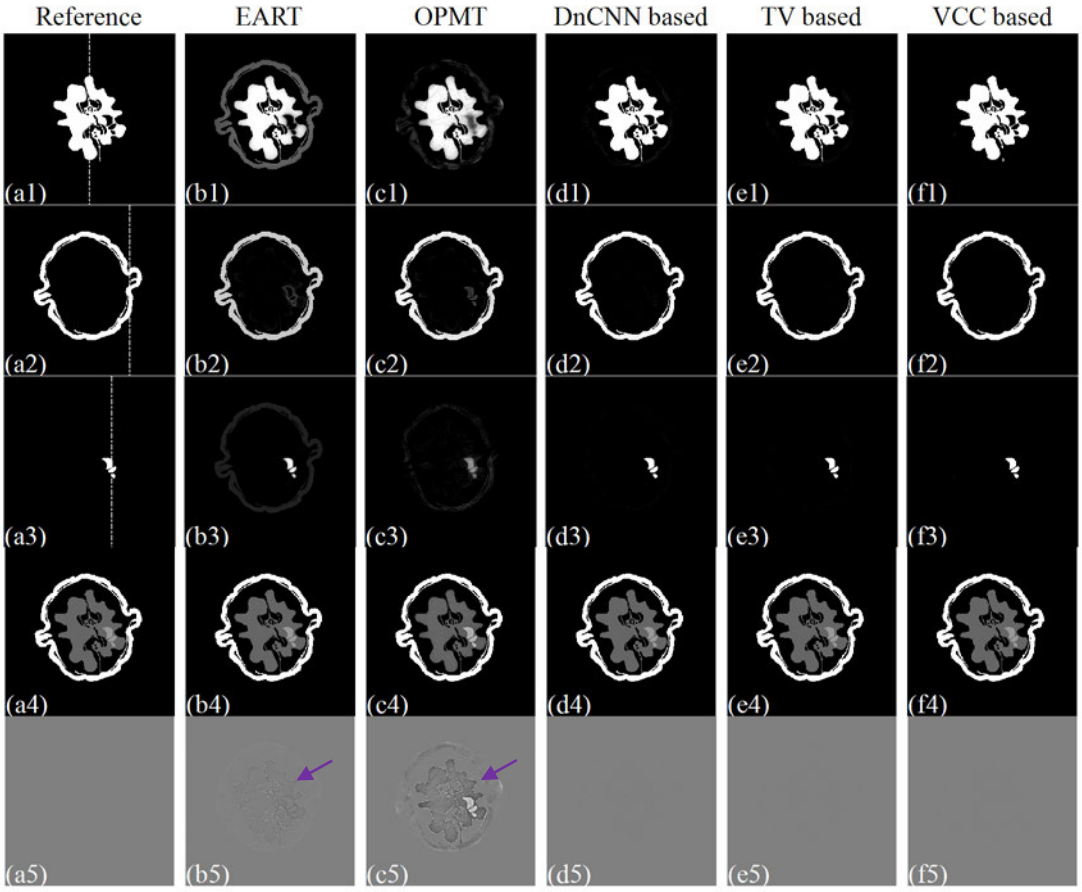

FIGURE 4. Results of simulation dataset obtained by different methods with noise (I_0 = 1e7). Columns (a) to (f) represent the Reference, EART method, OPMT method, DnCNN-based method, TV-based method, and VCC-based method, respectively. Rows from top to bottom indicate three materials: tissue, bone, iodine, the virtual monochromatic image at 75 keV, and the corresponding difference images, respectively, where the display windows of the display windows are [0.02 1], [0.01 1], [0.01 1], [0.001 0.055], and [−0.01, 0.01], respectively.

TABLE 1. Quantitative results of different methods.

Algorithm	Materials	Noisy(I_0 = 1e7)			Noisy(I_0 = 1e5)		
		PSNR	SSIM	RMSE	PSNR	SSIM	RMSE
EART	Tissue	19.677	0.882	1.04e-1	19.665	0.866	1.04e-1
	Bone	32.460	0.942	2.38e-2	31.105	0.934	2.78e-2
	Iodine	27.950	0.899	4.00e-2	27.976	0.899	3.99e-2
	Averaged	26.696	0.908	5.59e-2	26.249	0.899	5.72e-2
OPMT	Tissue	22.043	0.855	7.90e-2	18.721	0.817	1.16e-1
	Bone	30.568	0.952	2.96e-2	30.847	0.942	2.87e-2
	Iodine	27.335	0.847	4.30e-2	37.103	0.959	1.40e-2
	Averaged	26.649	0.884	5.05e-2	28.891	0.906	5.28e-2
DnCNN-based	Tissue	35.312	0.943	1.72e-2	27.088	0.901	4.42e-2
	Bone	40.833	0.991	9.09e-3	32.182	0.981	2.46e-2
	Iodine	42.551	0.969	7.45e-3	39.582	0.948	1.05e-2
	Averaged	39.566	0.968	1.12e-2	32.951	0.943	2.64e-2
TV-based	Tissue	41.939	0.967	8.00e-3	31.662	0.932	2.61e-2
	Bone	47.096	0.997	4.42e-3	45.671	0.998	5.21e-3
	Iodine	49.864	0.981	3.21e-3	48.694	0.973	3.68e-3
	Averaged	46.299	0.981	5.21e-3	42.009	0.968	1.17e-2
VCC-based	Tissue	53.669	0.999	2.07e-3	39.026	0.995	1.12e-2
	Bone	58.151	1	1.24e-3	45.837	0.999	5.11e-3
	Iodine	61.447	0.999	8.47e-4	56.656	1	1.47e-3

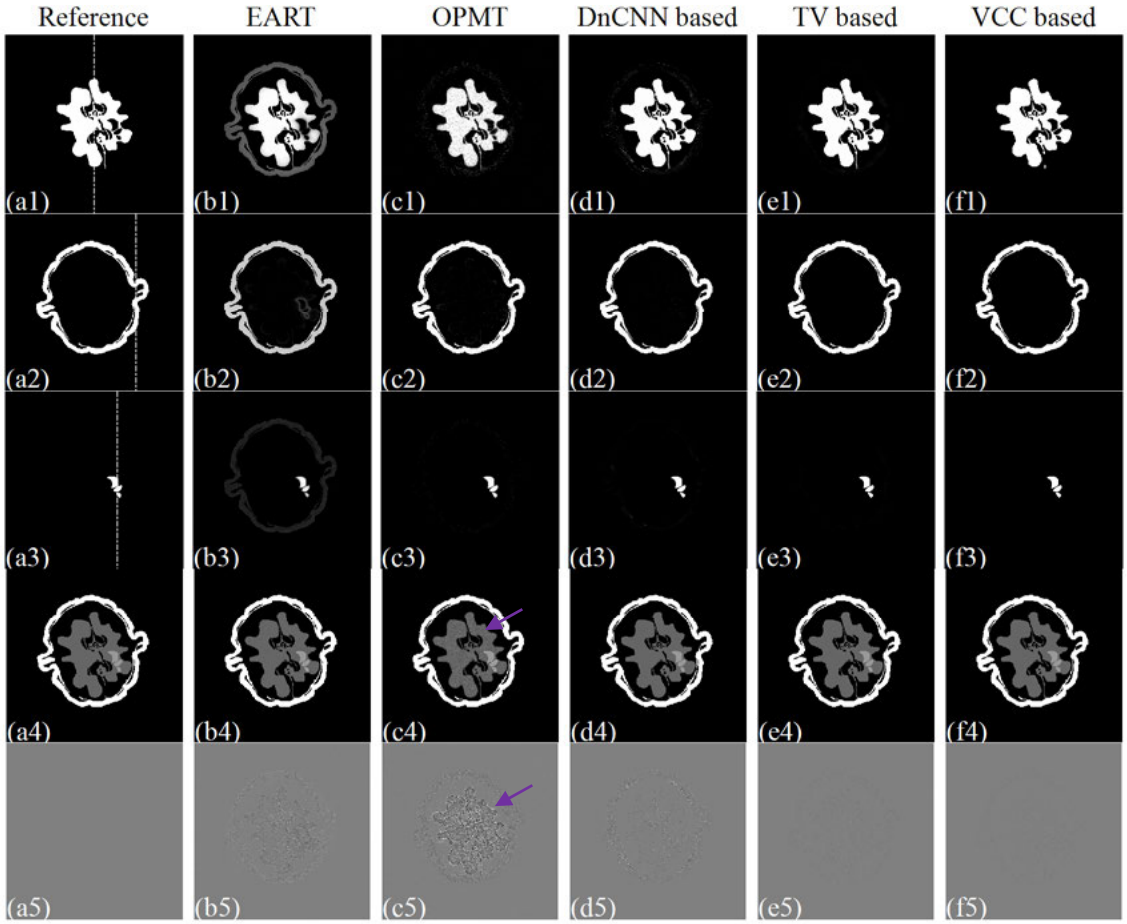

FIGURE 5. Results of simulation dataset obtained by different methods with noise (I_0 = 1e5). Columns (a) to (f) represent the Reference, EART method, OPMT method, DnCNN-based method, TV-based method, and VCC-based method, respectively. Rows from top to bottom indicate three materials: tissue, bone, iodine, the virtual monochromatic image at 75 keV, and the corresponding difference images, respectively, where the display windows of the display windows are [0.02 1], [0.01 1], [0.01 1], [0.001 0.055], and [−0.01, 0.01], respectively.

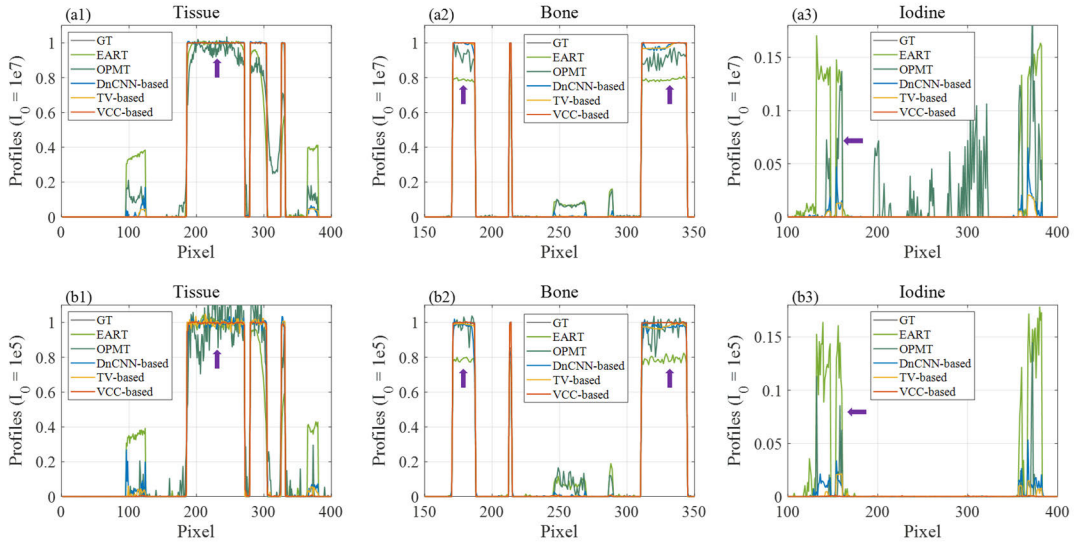

FIGURE 6. Profiles of different methods at different noise levels.

as 512 detector bins for the materials reconstruction in this experiment. The source to object and detector distances are 245.0 mm and 808.0 mm, respectively. The projections corresponding to the three X-ray scanning are obtained in an

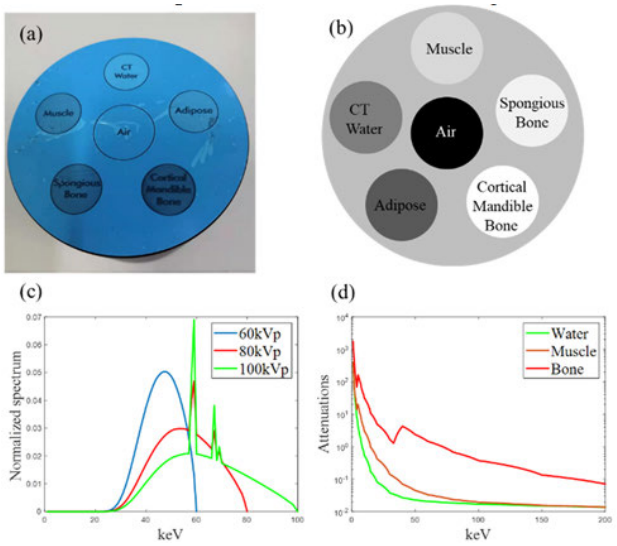

FIGURE 7. QRM phantom consists of five materials: cortical mandible bone, spongious bone, muscle, CT water, and adipose, where (a) represents the real QRM object; (b) represents the schematic diagram of five materials. And (c) plots the estimated three spectrums, (d) draws the linear attenuations of three basis materials.

alternating mode, i.e., the paths of rays are geometrically inconsistent. A total of 720 projection views are collected in the 360° range for each scanning.

The pixels of the reconstructed images are 512×512 with each size of 0.252×0.252 mm^2. And the spectrums are estimated by the expectation-maximization (EM) method [40], which shown in Figure 7 (c). The linear attenuations of three basis materials used in our experiments are drawn in Figure 7 (d). Some regions of interest (ROIs) (denoted in red dotted squares in Figure 8) are chosen to make quantitative evaluations of the mean value of attenuation coefficients and standard deviation (STD), which is calculated as follows

$$STD = \sqrt{\frac{1}{N_{roi}} \sum_{r=1}^{N_{roi}} (x_r - \bar{x})^2}, \tag{25}$$

where x_r denotes the value of r-th pixel. $\bar{x}$ is the pre-computed mean value of all N_{roi} image pixels of the selected ROI. And Some ROIs (denoted in yellow dotted squares in Figure 9) are magnified to assess the noise suppression across the different algorithms. Furthermore, the projection views are downsampled to 360 to assess the performance of the proposed methods.

Figure 8 shows the reconstructed results of all methods, where columns from (a) to (e) represent the EART method, OPMT method, DnCNN-based method, TV-based method, and VCC-based method, respectively. Rows from up to bottom represent the three materials, i.e., water, muscle, and bone. Note that the proposed VCC-based method chooses the spectrums generated by tube voltages 60 kVp and 100 kVp. As shown in Figure 8, all five methods can obtain the maps of three materials. However, due to the lack of denoising ability, some noises appear in the results reconstructed by EART and OPMT methods, which can be obviously seen from the reconstruction results of water basis material in Figure 8 (a1) and (b1), marked by purple arrows. And there are some other structures of muscle and water in the bone maps, as denoted by purple arrows in Figure 8 (a3) and (b3). The remaining three methods are all the methods proposed in this paper, and they have advantages in noise suppression to a certain extent. To further illustrate the effectiveness of the one-step method in eliminating beam-hardening artifacts, virtual monochromatic images are further shown in Figure 9. Figure 9 displays the results of virtual monochromatic images between the five iterative methods at single energy 70, and 110 keV, respectively. The results of EART and OPMT show that the reconstructed images are not smooth and uneven due to the existence of noise, especially in the region marked by purple arrows. Compared with the results reconstructed by EART and OPMT, the other three iterative one-step methods have abilities to suppress noises, as can be observed from the ROIs in Figure 9. The downsampled results of 360 projection views, shown in Figures 10 and 11, also have similar opinions.

Table 2 further lists the quantitative evaluations of different methods under 720 projection views, where the mean value is measured to assess the accuracy of the results, while the STD value evaluates the noise suppression ability of different methods. The STD values of the proposed methods also demonstrate that the proposed methods are superior in suppressing noises. The reference values of three ROIs are computed according to the threshold segmentation results of filtered backprojection algorithm reconstructions. From Table 2, the proposed methods have similar mean values in ROI 3 with other methods, indicating the accuracy of reconstruction results, while the STD values show the advantages of the proposed methods in ROI 1 and ROI 3 compared with other methods.

IV. DISCUSSIONS

In this paper, we consider the multi-material reconstruction problem in the case of each energy spectrum having an inconsistent scanning path. Note that the ill-condition of the multi-material reconstruction problem will be intensified with the increase of the number of materials, especially under inconsistent scanning geometry. The projection-domain methods don't work for the inconsistent path. It is more difficult to obtain accurate distributions of basis materials based on image-domain approaches when basis materials have similar attenuations. Aiming at this situation, a statistical multi-material based one-step reconstruction model is considered to describe more realistic distributions of photons. The model is firstly simplified by incorporating the statistical upper bound. Then, the fidelity data term further combines the sparsity-based TV regularization term and deep prior-based regularization term to integrate the noise suppression in each iteration of material reconstruction when the number of energies matches the number of materials. In addition, when the number of energies and the number of materials do not match, a new volume conservation

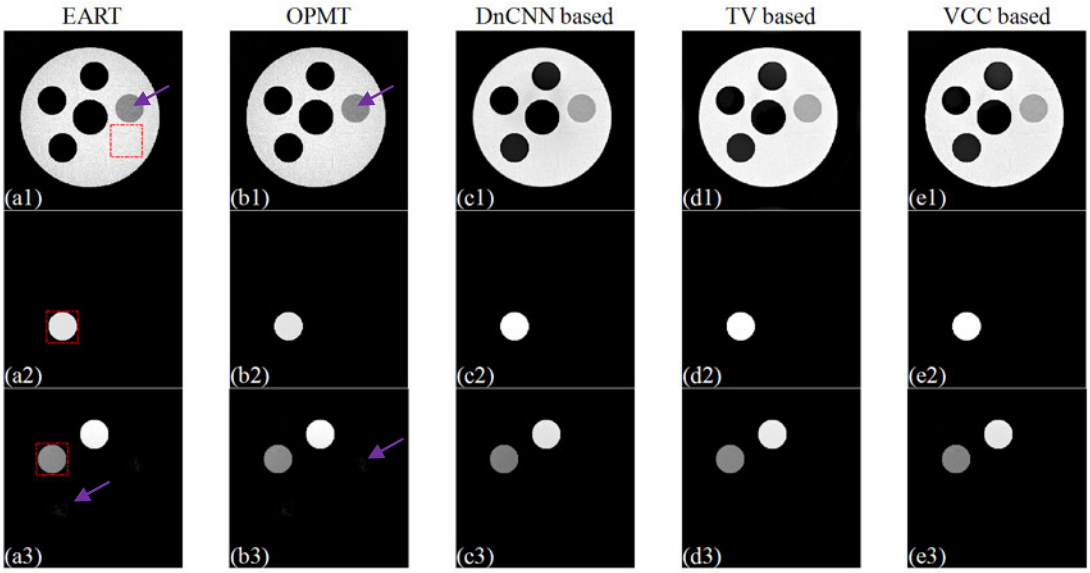

FIGURE 8. Reconstructed three material images of different methods under 720 projection views. Columns from (a) to (e) represent the EART method, OPMT method, DnCNN-based method, TV-based method, and VCC-based method, respectively. Rows from up to bottom represent water, muscle, and bone. And the corresponding display windows are [0 1.1], [0 0.5], and [0 0.04].

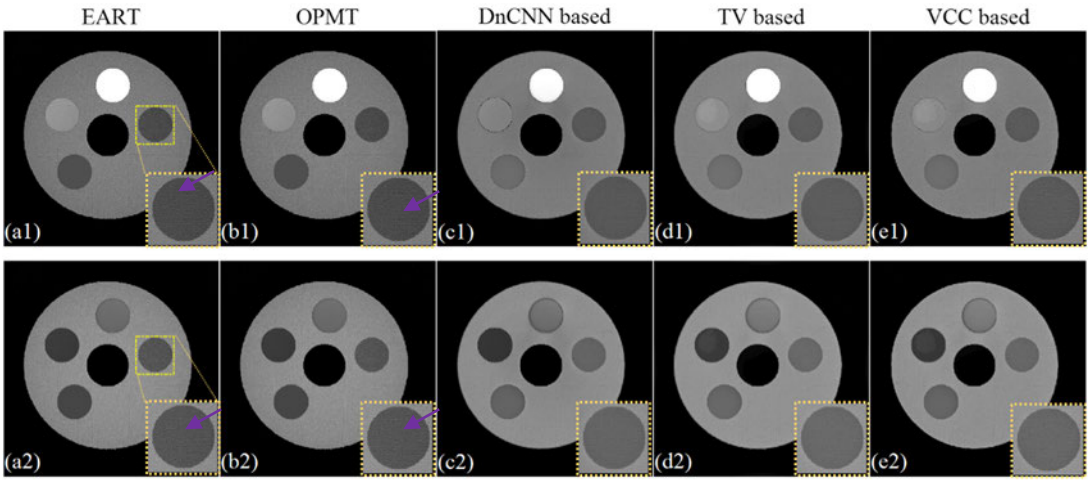

FIGURE 9. Virtual monochromatic images and the corresponding enlarged areas of different methods under 720 projection views. The first row represents the images at 70 keV and the second row represents the images at 110 keV. And the display windows are [0 0.04] and [0 0.03].

TABLE 2. The comparison of mean values and standard deviations for different methods.

	ROI	Reference	EART	OPMT	DnCNN-based	TV-based	VCC-based
720 views	1	1.005±0.063	1.005±0.063	1.005±0.063	0.9901±0.033	1.036±0.025	1.019±0.014
	2	0.284±0.211	0.282±0.214	0.283±0.214	0.324±0.246	0.323±0.245	0.317±0.240
	3	0.014±0.010	0.014±0.010	0.014±0.010	0.012±0.009	0.013±0.010	0.013±0.010

constraint is developed to improve the ill-condition of the inverse problem. Moreover, several numerical experiments are carried out to verify the effectiveness of the proposed methods. The results show that the practical performance is consistent with the original design, and it can obtain a relatively stable solution while suppressing noise. The monochromatic imaging results, as shown in Figure 9, further indicate the proposed method has the ability to suppress noise.

Although the proposed algorithms show that it is useful for multi-material reconstruction, model-driven methods based on certain assumptions cannot fully express the physical mechanism for the realistic application of CT imaging, for example, the response of detector units are different for

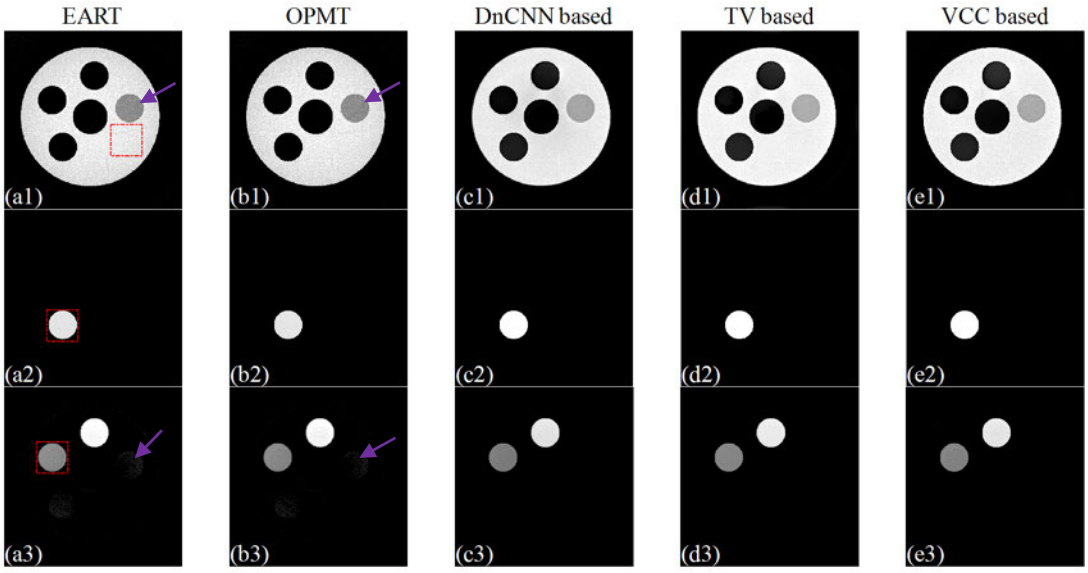

FIGURE 10. Reconstructed three material images of different methods under 360 projection views. Columns from (a) to (e) represent the EART method, OPMT method, DnCNN-based method, TV-based method, and VCC-based method, respectively. Rows from up to bottom represent water, muscle, and bone. And the corresponding display windows are [0 1.1], [0 0.5], and [0 0.04].

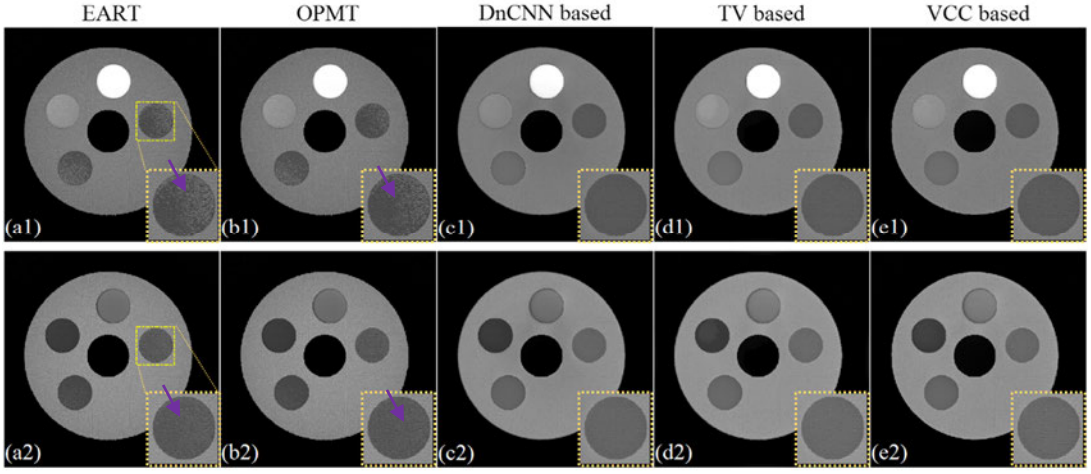

FIGURE 11. Virtual monochromatic images and the corresponding enlarged areas of different methods under 360 projection views. The first row represents the images at 70 keV and the second row represents the images at 110 keV. And the display windows are [0 0.04] and [0 0.03].

certain spectrum, and noise in the measured projections is easily multiple amplified in the reconstructed process of basis materials. The disturbance of noise is a huge instability factor for the convergence of the algorithm. As a result, data-driven methods for materials reconstruction have also been developed, such as Zhang et al. [41] proposed a butterfly network to realize material decomposition based on the image-domain under dual energy. Fang et al. applied the unsupervised denoising method called Noise2Noise [42] as the prior knowledge to estimate the material maps directly from the raw projection data [43]. And other researchers also find the deep learning-based method has certain advantages in medical image analysis [44], [45], [46], [47]. These methods also encourage us to combine model-driven and data-driven methods to achieve accurate decomposition of materials by eliminating the influence of beam-hardening artifacts while suppressing noise in the future.

V. CONCLUSION

For the inconsistent material-specific reconstruction, this paper applies a statistical model with different priors to establish material reconstruction models. First, the gradient sparsity-based and deep prior-based regularization terms are incorporated into the optimization problem to update the material maps when the numbers of materials and energies are consistent. Then, the volume conservation constraint is further added to improve the convergence rate when the numbers of materials and energies are not consistent. Furthermore,

the ordered subsets are applied to accelerate the proposed algorithms. The simulation and real data experiments verify the effectiveness of the proposed methods in basis material reconstruction, and also the capabilities in suppressing noise.

CONFLICT OF INTEREST

The authors have no conflicts of interest to declare.

ACKNOWLEDGMENT

The authors would like to thank the editors and the anonymous reviewers whose insightful comments have helped to improve the quality of this article considerably.

REFERENCES

[1] S. C. Brandelik, S. Skornitzke, T. Mokry, S. Sauer, W. Stiller, J. Nattenmüller, H. U. Kauczor, T. F. Weber, and T. D. Do, "Quantitative and qualitative assessment of plasma cell dyscrasias in dual-layer spectral CT," *Eur. Radiol.*, vol. 31, no. 10, pp. 7664–7673, Oct. 2021.

[2] W. Wu, D. Hu, K. An, S. Wang, and F. Luo, "A high-quality photon-counting CT technique based on weight adaptive total-variation and image-spectral tensor factorization for small animals imaging," *IEEE Trans. Instrum. Meas.*, vol. 70, pp. 1–14, 2021.

[3] S. Wang, W. Wu, J. Feng, F. Liu, and H. Yu, "Low-dose spectral CT reconstruction based on image-gradient L_0-norm and adaptive spectral PICCS," *Phys. Med. Biol.*, vol. 65, no. 24, Dec. 2020, Art. no. 245005.

[4] B. Daoud, J. Cazejust, S. Tavolaro, S. Durand, R. Pommier, A. Hamrouni, and G. Bornet, "Could spectral CT have a potential benefit in coronavirus disease (COVID-19)?" *Amer. J. Roentgenol.*, vol. 216, no. 2, pp. 349–354, Feb. 2021.

[5] A. Agostini, C. Floridi, A. Borgheresi, M. Badaloni, P. E. Pirani, F. Terilli, L. Ottaviani, and A. Giovagnoni, "Proposal of a low-dose, long-pitch, dual-source chest CT protocol on third-generation dual-source CT using a tin filter for spectral shaping at 100 kVp for CoronaVirus disease 2019 (COVID-19) patients: A feasibility study," *La Radiologia Medica*, vol. 125, no. 4, pp. 365–373, Apr. 2020.

[6] K. Taguchi and J. S. Iwanczyk, "Vision 20/20: Single photon counting X-ray detectors in medical imaging," *Med. Phys.*, vol. 40, no. 10, Oct. 2013, Art. no. 100901.

[7] N. G. Anderson, A. P. Butler, N. J. A. Scott, N. J. Cook, J. S. Butzer, N. Schleich, M. Firsching, R. Grasset, N. de Ruiter, M. Campbell, and P. H. Butler, "Spectroscopic (multi-energy) CT distinguishes iodine and barium contrast material in MICE," *Eur. Radiol.*, vol. 20, no. 9, pp. 2126–2134, Sep. 2010.

[8] J. Noh, J. A. Fessler, and P. E. Kinahan, "Statistical sinogram restoration in dual-energy CT for PET attenuation correction," *IEEE Trans. Med. Imag.*, vol. 28, no. 11, pp. 1688–1702, Nov. 2009.

[9] R. E. Alvarez, "Estimator for photon counting energy selective X-ray imaging with multibin pulse height analysis," *Med. Phys.*, vol. 38, no. 5, pp. 2324–2334, May 2011.

[10] T. Niu, X. Dong, and M. Petrongolo, "Iterative image-domain decomposition for dual-energy CT," *Med. Phys.*, vol. 41, no. 4, 2014, Art. no. 041901.

[11] C. Maaß, M. Baer, and M. Kachelrieß, "Image-based dual energy CT using optimized precorrection functions: A practical new approach of material decomposition in image domain," *Med. Phys.*, vol. 36, no. 8, pp. 3818–3829, 2009.

[12] Q. Ding, T. Niu, X. Zhang, and Y. Long, "Image-domain multimaterial decomposition for dual-energy CT based on prior information of material images," *Med. Phys.*, vol. 45, no. 8, pp. 3614–3626, Aug. 2018.

[13] R. E. Alvarez and A. Macovski, "Energy-selective reconstructions in X-ray computerised tomography," *Phys. Med. Biol.*, vol. 21, no. 5, pp. 733–744, 1976.

[14] A. Sawatsky, Q. Xu, C. O. Schirra, and M. A. Anastasio, "Proximal ADMM for multi-channel image reconstruction in spectral X-ray CT," *IEEE Trans. Med. Imag.*, vol. 33, no. 8, pp. 1657–1668, Aug. 2014.

[15] J. P. Schlomka, E. Roessl, R. Dorscheid, S. Dill, G. Martens, T. Istel, C. Bäumer, C. Herrmann, R. Steadman, G. Zeitler, A. Livne, and R. Proksa, "Experimental feasibility of multi-energy photon-counting K-edge imaging in pre-clinical computed tomography," *Phys. Med. Biol.*, vol. 53, no. 15, pp. 4031–4047, 2008.

[16] Z. Yu and D. S. Michael, "Analysis of fast kV-switching in dual energy CT using a pre-reconstruction decomposition technique," *Proc. SPIE*, vol. 6913, pp. 392–403, Mar. 2008.

[17] S. Faby, S. Kuchenbecker, S. Sawall, D. Simons, H.-P. Schlemmer, M. Lell, and M. Kachelrieß, "Performance of today's dual energy CT and future multi energy CT in virtual non-contrast imaging and in iodine quantification: A simulation study," *Med. Phys.*, vol. 42, no. 7, pp. 4349–4366, Jul. 2015.

[18] Y. Zhao, X. Zhao, and P. Zhang, "An extended algebraic reconstruction technique (E-ART) for dual spectral CT," *IEEE Trans. Med. Imag.*, vol. 34, no. 3, pp. 761–768, Mar. 2015.

[19] J. Hu, X. Zhao, and F. Wang, "An extended simultaneous algebraic reconstruction technique (E-SART) for X-ray dual spectral computed tomography," *Scanning*, vol. 38, no. 6, pp. 599–611, 2016.

[20] W. Zhang, S. Zhao, H. Pan, Y. Zhao, and X. Zhao, "An iterative reconstruction method based on monochromatic images for dual energy CT," *Med. Phys.*, vol. 48, no. 10, pp. 6437–6452, Oct. 2021.

[21] S. Zhao, H. Pan, W. Zhang, D. Xia, and X. Zhao, "An oblique projection modification technique (OPMT) for fast multispectral CT reconstruction," *Phys. Med. Biol.*, vol. 66, no. 6, Mar. 2021, Art. no. 065003.

[22] X. Qiong, M. Xuanqin, T. Shaojie, H. Wei, Z. Yizhai, and L. Tao, "Implementation of penalized-likelihood statistical reconstruction for polychromatic dual-energy CT," *Proc. SPIE*, vol. 7258, pp. 1666–1674, Mar. 2009.

[23] Y. Long and J. A. Fessler, "Multi-material decomposition using statistical image reconstruction for spectral CT," *IEEE Trans. Med. Imag.*, vol. 33, no. 8, pp. 1614–1626, Aug. 2014.

[24] T. Weidinger, T. M. Buzug, T. Flohr, S. Kappler, and K. Stierstorfer, "Polychromatic iterative statistical material image reconstruction for photon-counting computed tomography," *Int. J. Biomed. Imag.*, vol. 2016, Jan. 2016, Art. no. 5871604.

[25] K. Mechlem, S. Ehn, T. Sellerer, E. Braig, D. Münzel, F. Pfeiffer, and P. B. Noël, "Joint statistical iterative material image reconstruction for spectral computed tomography using a semi-empirical forward model," *IEEE Trans. Med. Imag.*, vol. 37, no. 1, pp. 68–80, Jan. 2018.

[26] R. F. Barber, E. Y. Sidky, T. G. Schmidt, and X. Pan, "An algorithm for constrained one-step inversion of spectral CT data," *Phys. Med. Biol.*, vol. 61, no. 10, pp. 3784–3818, 2016.

[27] R. F. Barber and E. Y. Sidky, "Convergence for nonconvex ADMM, with applications to CT imaging," 2020, *arXiv:2006.07278*.

[28] T. G. Schmidt, B. A. Sammut, R. F. Barber, X. Pan, and E. Y. Sidky, "Addressing CT metal artifacts using photon-counting detectors and one-step spectral CT image reconstruction," *Med. Phys.*, vol. 49, no. 5, pp. 3021–3040, May 2022.

[29] C. Cai, T. Rodet, S. Legoupil, and A. Mohammad-Djafari, "A full-spectral Bayesian reconstruction approach based on the material decomposition model applied in dual-energy computed tomography," *Med. Phys.*, vol. 40, no. 11, p. 111916, 2013.

[30] Q. Xu, A. Sawatzky, M. A. Anastasio, and C. O. Schirra, "Sparsity-regularized image reconstruction of decomposed K-edge data in spectral CT," *Phys. Med. Biol.*, vol. 59, no. 10, pp. N65–N79, May 2014.

[31] B. Chen, Z. Zhang, E. Y. Sidky, D. Xia, and X. Pan, "Image reconstruction and scan configurations enabled by optimization-based algorithms in multispectral CT," *Phys. Med. Biol.*, vol. 62, no. 22, pp. 8763–8793, Nov. 2017.

[32] B. Chen, Z. Zhang, D. Xia, E. Y. Sidky, and X. Pan, "Non-convex primal-dual algorithm for image reconstruction in spectral CT," *Computerized Med. Imag. Graph.*, vol. 87, Jan. 2021, Art. no. 101821.

[33] W. Zhang, A. Cai, Z. Zheng, L. Wang, N. Liang, L. Li, B. Yan, and G. Hu, "A direct material reconstruction method for DECT based on total variation and BM3D frame," *IEEE Access*, vol. 7, pp. 138579–138592, 2019.

[34] K. Zhang, W. Zuo, Y. Chen, D. Meng, and L. Zhang, "Beyond a Gaussian denoiser: Residual learning of deep CNN for image denoising," *IEEE Trans. Image Process.*, vol. 26, no. 7, pp. 3142–3155, Jul. 2017.

[35] S. V. Venkatakrishnan, C. A. Bouman, and B. Wohlberg, "Plug-and-play priors for model based reconstruction," in *Proc. IEEE Global Conf. Signal Inf. Process. (GlobalSIP)*, Dec. 2013, pp. 945–948.

[36] J. S. Jørgensen and E. Y. Sidky, "How little data is enough? Phase-diagram analysis of sparsity-regularized X-ray computed tomography," *Phil. Trans. Roy. Soc. A, Math., Phys. Eng. Sci.*, vol. 373, no. 2043, Jun. 2015, Art. no. 20140387.

[37] Z. Wang, A. C. Bovik, H. R. Sheikh, and E. P. Simoncelli, "Image quality assessment: From error visibility to structural similarity," *IEEE Trans. Image Process.*, vol. 13, no. 4, pp. 600–612, Apr. 2004.
[38] H. Erdogan and J. A. Fessler, "Ordered subsets algorithms for transmission tomography," *Phys. Med. Biol.*, vol. 44, no. 11, pp. 2835–2851, Nov. 1999.
[39] G. Poludniowski, G. Landry, F. DeBlois, P. M. Evans, and F. Verhaegen, "SpekCalc: A program to calculate photon spectra from tungsten anode X-ray tubes," *Phys. Med. Biol.*, vol. 54, no. 19, pp. N433–N438, Oct. 2009.
[40] E. Y. Sidky, L. Yu, X. Pan, Y. Zou, and M. Vannier, "A robust method of X-ray source spectrum estimation from transmission measurements: Demonstrated on computer simulated, scatter-free transmission data," *J. Appl. Phys.*, vol. 97, no. 12, 2005, Art. no. 124701.
[41] W. Zhang, H. Zhang, L. Wang, X. Wang, X. Hu, A. Cai, L. Li, T. Niu, and B. Yan, "Image domain dual material decomposition for dual-energy CT using butterfly network," *Med. Phys.*, vol. 46, no. 5, pp. 2037–2051, 2019.
[42] J. Lehtinen, J. Munkberg, J. Hasselgren, S. Laine, T. Karras, M. Aittala, and T. Aila, "Noise2Noise: Learning image restoration without clean data," 2018, *arXiv:1803.04189*.
[43] W. Fang, D. Wu, K. Kim, M. K. Kalra, R. Singh, L. Li, and Q. Li, "Iterative material decomposition for spectral CT using self-supervised Noise2Noise prior," *Phys. Med. Biol.*, vol. 66, no. 15, Aug. 2021, Art. no. 155013.
[44] S. Wang, H. Yu, Y. Xi, C. Gong, W. Wu, and F. Liu, "Spectral-image decomposition with energy-fusion sensing for spectral CT reconstruction," *IEEE Trans. Instrum. Meas.*, vol. 70, pp. 1–11, 2021.
[45] T. Zhang, H. Yu, Y. Xi, S. Wang, and F. Liu, "Spectral CT image-domain material decomposition via sparsity residual prior and dictionary learning," *IEEE Trans. Instrum. Meas.*, vol. 72, pp. 1–13, 2023.
[46] W. Wu, X. Guo, Y. Chen, S. Wang, and J. Chen, "Deep embedding-attention-refinement for sparse-view CT reconstruction," *IEEE Trans. Instrum. Meas.*, vol. 72, pp. 1–11, 2023.
[47] S. Wang, W. Wu, A. Cai, Y. Xu, V. Vardhanabhuti, F. Liu, and H. Yu, "Image-spectral decomposition extended-learning assisted by sparsity for multi-energy computed tomography reconstruction," *Quant. Imag. Med. Surg.*, vol. 13, no. 2, pp. 610–630, Feb. 2023.

XIAOHUAN YU received the M.S. degree from Zhengzhou University, Zhengzhou, China. She is currently pursuing the Ph.D. degree with the College of Information Engineering, PLA Strategic Support Force Information Engineering University, Zhengzhou. Her research interests include the theory and application of imaging, especially on intelligent algorithms for inverse problems, image processing, spectral computed tomography, and its applications on biomedical and industrial fields.

AILONG CAI received the B.S., M.S., and Ph.D. degrees from the College of Information Engineering, PLA Strategic Support Force Information Engineering University, Zhengzhou, China, in 2011, 2014, and 2018, respectively. He is currently an Associate Professor with the College of Information Engineering and the Henan Key Laboratory of Imaging and Intelligent Processing, PLA Strategic Support Force Information Engineering University. His research interests include the theory and application of imaging, especially on intelligent algorithms for inverse problems, image processing, spectral computed tomography, and its applications on biomedical and industrial fields.

NINGNING LIANG was born in Tianjin, China, in 1982. She received the B.S., M.S., and Ph.D. degrees from the PLA Strategic Support Force Information Engineering University, Zhengzhou, China, in 2004, 2009, and 2015, respectively. She is currently an Associate Professor with the PLA Strategic Support Force Information Engineering University and the Deputy Director of the Henan Key Laboratory of Imaging and Intelligent Processing. Her research interests include X-ray CT system design and intelligent image processing.

SHAOYU WANG was born in Nanyang, Henan, China, in 1992. He received the M.S. and Ph.D. degrees from Chongqing University, Chongqing, in 2018 and 2021, respectively. From 2019 to 2020, he was a joint-training Ph.D. Student with the University of Massachusetts Lowell. He is currently a Lecturer with the College of Information Engineering, PLA Strategic Support Force Information Engineering University. His research interests include X-ray system design, image reconstruction, and material decomposition. He received the scholarship from the Chinese Scholarship Council, in 2019.

LEI LI received the B.S., M.S., and Ph.D. degrees from the College of Information Engineering, PLA Strategic Support Force Information Engineering University, Zhengzhou, China, in 2003, 2006, and 2016, respectively. He is currently an Associate Professor with the College of Information Engineering and the Henan Key Laboratory of Imaging and Intelligent Processing, PLA Strategic Support Force Information Engineering University. His research interests include the theory, technology, and application of imaging, especially on X-ray system design, spectral computed tomography, and its applications on biomedical and industrial fields.

BIN YAN received the Ph.D. degree in physics from the Chinese Academy of Sciences, in 2005. He is currently a Professor with the College of Information Engineering, PLA Strategic Support Force Information Engineering University. His research interests include the theory and application of computed tomography imaging, computer vision, and brain–computer interaction.